PAPER

Synergizing superresolution optical fluctuation imaging with single molecule localization microscopy

Methods and Applications in Fluorescence

PAPER

Synergizing superresolution optical fluctuation imaging with single molecule localization microscopy

Shachar Schidorsky[1,3], **Xiyu Yi**[2,3], **Yair Razvag**[1], **Julia Sajman**[1], **Kobi Hermon**[1], **Shimon Weiss**[2] and **Eilon Sherman**[1]

[1] Racah Institute of Physics, The Hebrew University, Jerusalem, Israel, 91904
[2] Department of Chemistry & Biochemistry, UCLA, CA, United States of America, 90095-1569
[3] Equal contribution.

RECEIVED
3 May 2018

REVISED
7 August 2018

ACCEPTED FOR PUBLICATION
22 August 2018

PUBLISHED
18 September 2018

Keywords: Super resolution microscopy, single molecule localization microscopy (SMLM), super-resolution optical fluctuation imaging (SOFI), photoactivated localization microscopy (PALM), direct stochastic optical reconstruction microscopy (dSTORM)

Supplementary material for this article is available online

Abstract

Single-molecule-localization-microscopy (SMLM) and superresolution-optical-fluctuation-imaging (SOFI) enable imaging biological samples well beyond the diffraction-limit of light. SOFI imaging is typically faster, yet has lower resolution than SMLM. Since the same (or similar) data format is acquired for both methods, their algorithms could presumably be combined synergistically for reconstruction and improvement of overall imaging performance. For that, we first defined a measure of the acquired-SNR for each method. This measure was ~x10 to x100 higher for SOFI as compared to SMLM, indicating faster recognition and acquisition of features by SOFI. This measure also allowed fluorophore-specific optimization of SOFI reconstruction over its time-window and time-lag. We show that SOFI-assisted SMLM imaging can improve image reconstruction by rejecting common sources of background (e.g. out-of-focus emission and auto-fluorescence), especially under low signal-to-noise ratio conditions, by efficient optical sectioning and by shortening image reconstruction time. The performance and utility of our approach was evaluated by realistic simulations and by SOFI-assisted SMLM imaging of the plasma membrane of activated fixed and live T-cells (in isolation or in conjugation to antigen presenting cells). Our approach enhances SMLM performance under demanding imaging conditions and could set an example for synergizing additional imaging techniques.

Introduction

Multiple super-resolution microscopy (SRM) techniques currently enable imaging biological samples well beyond the diffraction limit of light [1]. Such techniques may vary significantly not only in their spatial and temporal resolutions, but also in their performance with regard to background rejection, photobleaching, and potential image reconstruction artifacts. For instance, single molecule localization microscopy (SMLM) techniques such as Photoactivated Localization Microscopy (PALM) [2] and (direct) Stochastic Optical Reconstruction Microscopy (dSTORM) [3, 4] can localize single molecules with resolution down to ~10–20 nm, but require thousands of frames for the collection of data for a single image (e.g. [2]). In contrast, methods such as Stimulated Emission Depletion (STED) [5], Structured Illumination Microscopy (SIM) [6] and nonlinear SIM [7] perform measurements on ensembles of fluorophores, and provide spatial resolution of ~10–100 nm [1]. Also, in contrast to SMLM, STED requires spatial scanning, while SIM and nonlinear SIM require scanning of spatial illumination frequencies and their orientation.

SMLM and super-resolution optical fluctuation imaging (SOFI) [8] typically share a wide-field imaging configuration and use the reversible blinking of fluorophores for generating a super-resolved image. Thus, these techniques can be applied to the same data set. However, different fluorophore densities and signal-to-noise ratios (SNRs) are required for their respective optimal performances [9]. Nonetheless, we argue, and demonstrate below, that these methods could be

combined synergistically to improve overall imaging performance. Specifically, we focus here on merging the techniques of either PALM or dSTORM with SOFI [8]. We found that image reconstruction by SOFI converges much faster than by SMLM in its ability to detect resolution-unlimited features, and that it provides information that is complementary to SMLM. Moreover, we show that SOFI could efficiently reject background in SMLM reconstruction. Our approach was validated by running the SOFI-assisted SMLM reconstruction code both on realistic simulations and on experimental data taken on T cell activation markers at the plasma membrane of fixed and live T-cells (in isolation or in conjugation to antigen presenting cells). SOFI-assisted SMLM reconstruction significantly enhances SMLM performance under demanding imaging conditions and sets an example for synergizing other SRM techniques.

Results

Image acquisition requires time for the collection of information. Super resolution imaging increases the extent of acquired information in the image and thus, takes longer to acquire than diffraction limited imaging techniques [10]. To compare the time-dependent image build-up of SOFI and PALM, we dropped T-cells expressing Dronpa-actin on activating αCD3-coated coverslip, let them spread for 3 min and fixed them. We then imaged the cells using PALM in total internal reflection fluorescence (TIRF) mode (see Methods in the SI, and [11] for further details). Figure 1(A) shows the time-dependent image build-up using either 2nd order SOFI (top row) [12] or PALM (bottom row) image reconstruction of the footprint of the cells. The pronounced actin ring at the cell interface with the coverslip is a hallmark of T cell activation [13, 14]. It becomes almost immediately visible by diffraction limited microscopy (frame 40), next it becomes visible via SOFI image reconstruction (frames 40–200), but takes longer to show as a continuous feature via PALM image reconstruction (frames 400–1200).

Figure 1(B) shows the time-dependent image build-up using either 2nd order SOFI (top row) or dSTORM (bottom row) image reconstruction of phosphorylated ZAP70 (pZAP70) of a fixed T cell stained with Alexa647 via immune-staining. ZAP70 plays an important role in T cell antigen receptor (TCR) signalling process and shows pronounced sub-diffraction clusters at the plasma membrane (PM) that form as a result of T cell activation [15]. The features of pZAP70 converge faster in SOFI image reconstruction than in dSTORM reconstruction (compare their corresponding images at figure 1(B), frame 40), but reach higher spatial resolution for dSTORM. Thus, more generally, SOFI image reconstruction seem to converge faster than SMLM imaging [9], while SMLM reaches higher resolution enhancement than SOFI.

We note that the visual assessment of the build-up time of distinct features in the images of figures 1(A), (B) can be highly subjective. To overcome this issue and enable a more quantitative comparison of the temporal acquisition speed of SOFI and SMLM, we propose below a statistical measure and discuss its results (and limitations) when applied to the presented images in figure 1.

The acquisition efficiency of SOFI and SMLM

Signal to Noise Ratio (SNR) is a commonly used figure of merit (FOM) in image processing as a practical measure of image quality for the detection of objects or features on a randomly fluctuating background [16]. A common definition is given by [17]:

$$SNR = \frac{\mu_s}{Std(B)} = \frac{\frac{1}{N}\sum_{x,y}(I(x,y) - B(x,y))}{Std(B(x,y))} \quad (1)$$

where μ_s is the average signal, $Std(B)$ is the spatial standard deviation of the background (B), I is the intensity and N is the number of pixels with coordinates (x, y) in a specific region of interest (ROI) where the signal is detected from a user-defined feature of interest.

We note issues with the typical use of SNR as an FOM. First, it is hard to separate the local background from the signal of interest, as it exists in each pixel that contains signal. One way to quantify the SNR utilizes the Jackknife (delete-1) method [18]. Using this method for the SOFI analysis (figures 1(A), (B) bottom rows), we obtained an SNR of 6–8 that increases with the number of acquired frames (figures S1(A), (B) is available online at stacks.iop.org/MAF/6/045008/mmedia). The Jackknife method cannot be applied directly to the intensity of the detected peaks in SMLM [19]. Still, their local SNR is readily obtained by comparing the total intensity of each detected peak to its immediate background. Using this approach, we note that the SNR of the detected peaks in our assays averaged at ~2 for both our PALM and dSTORM images (figures S1(E), (F); related to figures 1(A), (B) top rows). As an alternative to the Jackknife approach for assessing the background and noise, one can define an ROI that clearly lies outside the feature of interest and quantify the background and noise there (figure 2(B)).

A second problem with the typical calculation of SNR is that it is typically derived from the fully processed image. However, such processing often incorporates non-linear and subjective thresholding. Such is typically the case in SMLM [2], but not in SOFI [8]. Thus, desired (and even erroneous) SNR values may be obtained at will, and direct comparison of the SNR of SMLM and wide field imaging results (e.g. SOFI or standard sum intensity imaging) could be meaningless. For instance, consider SMLM filtering (e.g. using intensity thresholding) that eliminates all of the false detections from the background, while leaving only a few detections from the

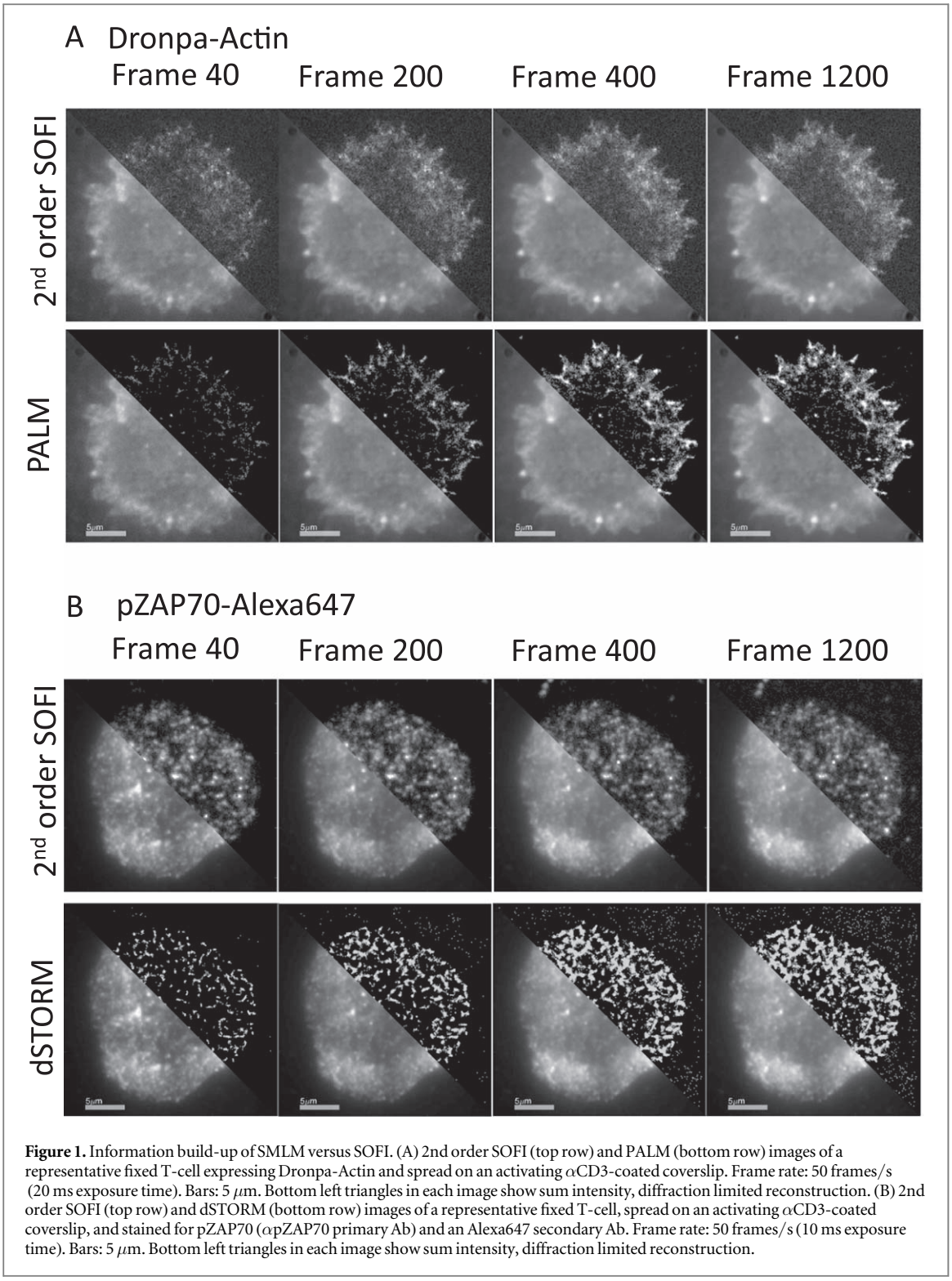

Figure 1. Information build-up of SMLM versus SOFI. (A) 2nd order SOFI (top row) and PALM (bottom row) images of a representative fixed T-cell expressing Dronpa-Actin and spread on an activating αCD3-coated coverslip. Frame rate: 50 frames/s (20 ms exposure time). Bars: 5 μm. Bottom left triangles in each image show sum intensity, diffraction limited reconstruction. (B) 2nd order SOFI (top row) and dSTORM (bottom row) images of a representative fixed T-cell, spread on an activating αCD3-coated coverslip, and stained for pZAP70 (αpZAP70 primary Ab) and an Alexa647 secondary Ab. Frame rate: 50 frames/s (10 ms exposure time). Bars: 5 μm. Bottom left triangles in each image show sum intensity, diffraction limited reconstruction.

feature of interest. Such filtering would result in an infinite SNR, according to equation (1).

To minimize bias through signal thresholding and related non-linear processing, we introduce a modified SNR as an FOM. This FOM quantifies the SNR on the *detected signals* of a feature of interest without further processing, as explained below. It is constructed to highlight specific differences in the acquisition process of SOFI and SMLM and their implications on the effective acquisition rates of these two imaging methods.

To construct this FOM, we first separate the process of image acquisition and processing (by an arbitrary method) into three steps that result in the following reconstructions (figure 2(A)): (1) Raw intensity → (2) Processed signal and related background → (3) Fully processed image after non-linear thresholding and filtering. We also note that both SMLM and SOFI are calculated over a time window containing multiple frames. Thus, we define the acquired SNR (ASNR) as follows:

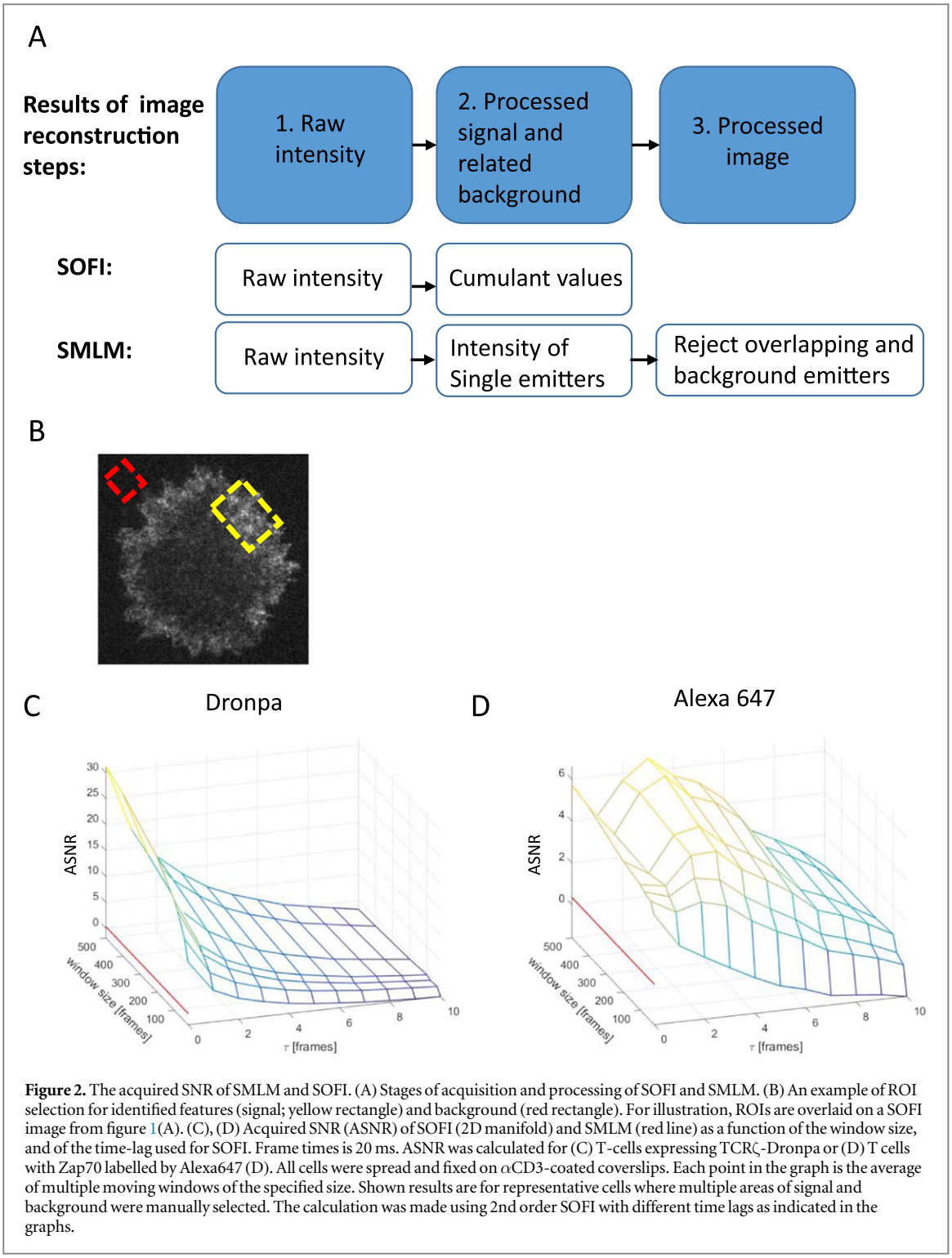

Figure 2. The acquired SNR of SMLM and SOFI. (A) Stages of acquisition and processing of SOFI and SMLM. (B) An example of ROI selection for identified features (signal; yellow rectangle) and background (red rectangle). For illustration, ROIs are overlaid on a SOFI image from figure 1(A). (C), (D) Acquired SNR (ASNR) of SOFI (2D manifold) and SMLM (red line) as a function of the window size, and of the time-lag used for SOFI. Frame times is 20 ms. ASNR was calculated for (C) T-cells expressing TCRζ-Dronpa or (D) T cells with Zap70 labelled by Alexa647 (D). All cells were spread and fixed on αCD3-coated coverslips. Each point in the graph is the average of multiple moving windows of the specified size. Shown results are for representative cells where multiple areas of signal and background were manually selected. The calculation was made using 2nd order SOFI with different time lags as indicated in the graphs.

$$ASNR(feature,\ window) = SNR(step\ 2, feature, window) = \frac{1/N\sum(S(step\ 2, feature, window) - \langle B(step\ 2, feature, window)\rangle)}{Std(B(step\ 2, feature, window))} \quad (2)$$

where '*window*' represents a part of the frames on which the data (including both signal and background) is processed. Integration is performed here over all pixels of the feature of interest and all frames of the time window. Thus, N is the total number of pixels in a specific ROI that contains the feature, multiplied by the number of frames.

Figures 2(C) and (D) show the ASNR of user-defined ROIs that include features within cells. The cells were labelled with either Dronpa or Alexa 647

respectively. The ASNR for SOFI is shown as a 2D manifold, as a function of the window size and the time lag τ that were used for SOFI reconstruction. The ASNR for SMLR is shown as a function of the window size (red line). Note that the ASNR values for SOFI and SMLM both depend on the specific fluorophore used (compare panels C and D in figure 2). Also note that optimal ASNR for SOFI is achieved when using $\tau = 0$ frames for Dronpa and $\tau = 2$ *or* 3 frames for Alexa 647 (at a frame time of 20msec). This holds true for most window sizes. Thus, SOFI reconstruction and its optimal time-lag clearly depend on the specific fluorophore used for imaging. Interestingly, such a difference in the optimal time lag for SOFI reconstruction was not detected through the Jackknife SNR statistics (figures S1(C), (D)), and to the best or our knowledge, has not been thoroughly considered and discussed in SOFI-related publications before.

We next simulated fluorophores with different photophysical properties to study their effect on the optimal time lag for SOFI reconstruction (see SI-2.7 for further details). Specifically, we fixed the on-time of fluorophore blinking at three different values (20, 100 and 500 ms) and considered for each on-time a range of blinking off-times (between 10 ms and 900 ms). The simulations of each fluorophore type resulted in movies that were reconstructed using SOFI with a time lag of either 0 or 1 (figures S2(C)–(E)). We found that for the shortest on-time, the optimal time lag was always 0 (figure S2(C)). However, for the longer on-times, the optimal time lag switched from 0 to 1 at specific off-times (figures S2(D), (E)). These results were independent on the window sizes, ranging between 50 and 500 frames (data is shown for window size of 350 frames). We conclude that the difference in the optimal time lag for SOFI reconstruction of Dronpa and Alexa647 originates from their different photophysical properties and blinking statistics. We next used the fluorophore-specific optimal time-lag for SOFI reconstruction throughout this study.

The ASNR of SOFI grows monotonically with the increase of window size in all cases. Therefore, to obtain optimal SOFI reconstruction, one should balance the window size with the desired temporal resolution, esp. for live-cell imaging. We find that ASNR for SMLM is much lower than the ASNR for SOFI and is effectively constant for the shown range of window sizes (figures 2(C), (D)). We obtain ASNR values of 0.31 ± 0.01 for Dronpa and 0.35 ± 0.01 for Alexa 647. SOFI has about ~1–2 orders of magnitude higher ASNR values than SMLM. This means that the acquired SNR of SOFI-reconstructed features builds-up faster than for SMLM. Since visibility is directly related to SNR [20], this property of SOFI reconstruction further allows the faster build-up of (resolution-unlimited) feature visibility, relative to SMLM reconstruction. To show this faster build up by SOFI, we calculated the ASNR for SOFI and SMLM over time (20–1500 frames, at 20msec per frame). Indeed, the SOFI ASNR for either Dronpa or Alexa 647 was higher than the SMLM ASNR throughout the acquisition time (figures S2(A), (B)). However, SOFI decoded features are limited in their spatial resolution (~100 nm for visible light and 2nd order reconstruction [8]) while SMLM achieves single molecule localization data with spatial resolution of ~20 nm [2–4].

SOFI can be used for SMLM background rejection

To explore possible synergies between two imaging techniques, it is useful to compare their results first. An effective way for evaluating differences between two imaging techniques is to pixel-wise compare parameters of the reconstructed images. Particularly, the statistical dependence of SMLM parameters (that are characteristic of peak centroids) on 2nd order SOFI pixel value, in which SMLM peaks are found, can be assessed by plotting 2D scatter plots of SMLM parameters versus SOFI pixel values (figure 3(A)). For SMLM, such parameters included the localization statistics of SMLM peaks (variance σ and localization uncertainty $\hat{\sigma}_{x,y}$), their intensities, and their local background statistics. For analysis, we either used the PALM data of T cells expressing Dronpa-actin (figure 1(A)) or dSTORM images of T cells stained for pZAP70 (figure 1(B)). For SOFI, each pixel value reports on the extent of temporal correlation of intensity fluctuations of the pixel [8]. Note that SOFI pixel values often originate from a superposition of fluctuating signals from multiple emitters. The same emitters would result in multiple SMLM localizations within that pixel or in its vicinity, but on a much finer grid. The 2D scatter plots of figure 3 show that SOFI values do not correlate well with any of the SMLM localization parameters (for PALM see figures 3(A) and (B) and for dSTORM see figures 3(C) and (D)). The Pearson correlation values of SMLM detection parameters and the SOFI pixel values in figure 3 are summarized in table S1. This table shows very low correlations (Pearson value of ~0) for either Dronpa or Alexa647 for the SMLM total detection intensity, Gaussian width of the peak (σ) and the localization uncertainty ($\sigma_{x,y}$). Still, limited correlation (Pearson value of 0.2–0.5) is detected for background related parameters (offset and std) and SOFI pixel values.

The low correlation in the pixel-wise comparison of SOFI and SMLM indicates that SOFI may contribute information on the temporal fluctuations of emitters that is missing in the SMLM analyses, and thus enhance these analyses. Importantly, we find that the combined information from SOFI and SMLM allows for efficient isolation and classification of different emitter types in the sample, and most importantly, the efficient separation of background from signal. For example, the green dots in figure 3(A) highlight the cell footprint, where Dronpa-actin can be identified, while blue dots mark false localizations from the background, outside of the

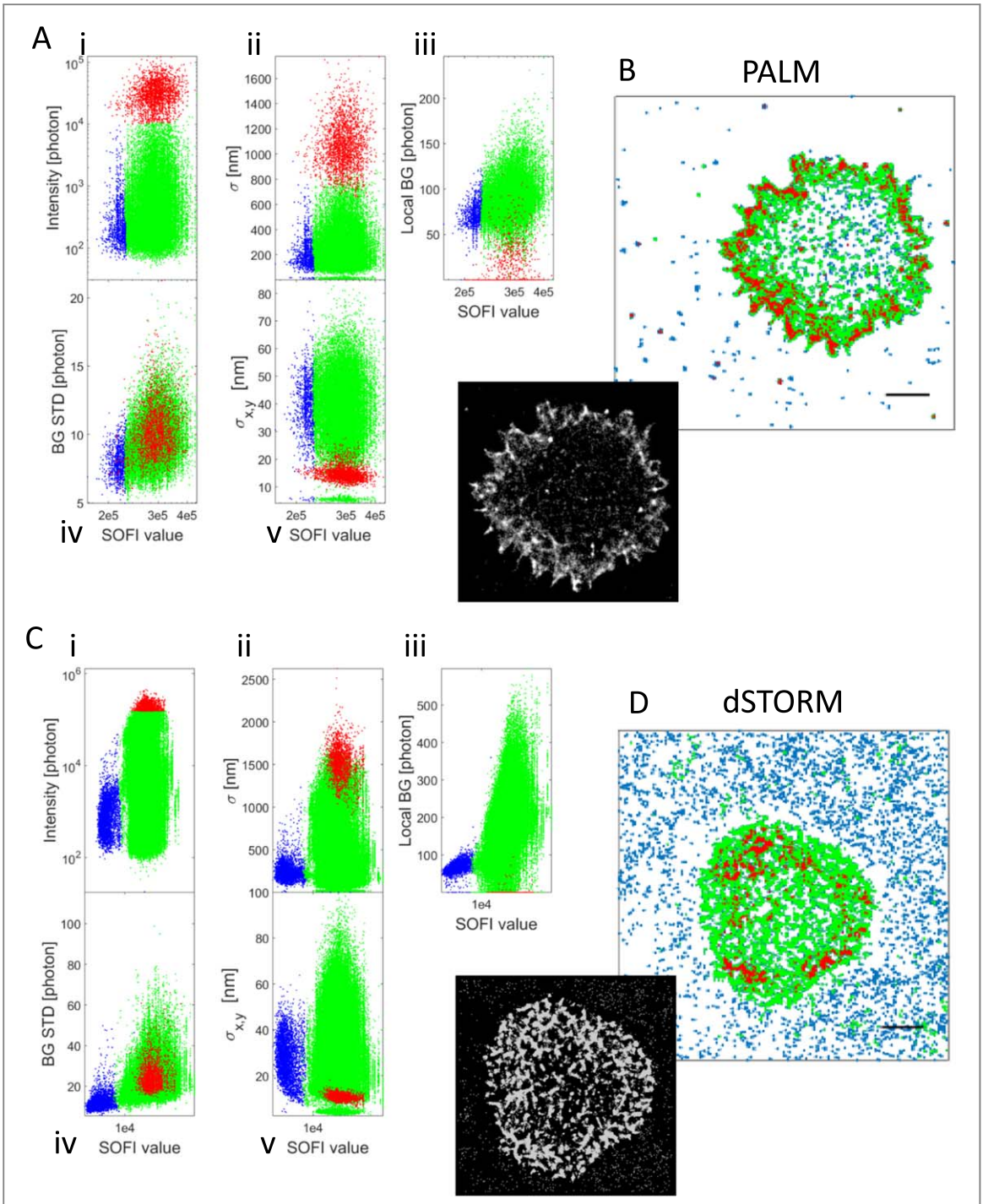

Figure 3. SOFI-assisted SMLM. (A) Scatter plots of various PALM localization parameters of localizations within a given pixel versus SOFI value of the same pixel (plotted for all pixels). Localization parameters include (i) the PSF width (σ), (ii) the intensity (total number of photons) of the fitted Gaussian, (iii) the local background (BG), (iv) background standard-deviation (STD), and (v) the localization uncertainty ($\hat{\sigma}_{x,y}$). Data was analyzed from a movie (same as figure A) of a single representative cell presented in figure 1(A). Manual classification of points was applied to two subpopulations of localizations in the A_i scatter plot (intensity versus SOFI value) (red and green dots; blue dots represent all localizations). This colouring was next applied to all localizations in all other scatter plots $A_{ii} - A_v$ and for (B) the corresponding PALM image. Pearson correlation values of the data in panel A are shown in table S1. (C) Scatter plots of various dSTORM localization parameters of localizations within a given pixel versus SOFI value of the same pixel (plotted for all pixels). Localization parameters include (i) the PSF width (σ), (ii) the intensity of the fit Gaussian, (iii) the local background (BG), (iv) background standard-deviation (STD), and (v) the localization uncertainty ($\hat{\sigma}_{x,y}$). Data was analyzed from a movie 50 frames/s (10 ms exposure time) of a single representative T cell spread on an activating αCD3-coated coverslip and stained with an αpZAP70-Alexa647 antibody. Manual classification of points was applied to two subpopulations of localizations in the C_i scatter plot (intensity versus SOFI value) (red and green dots; blue dots represent all localizations). This colouring was next applied to all localizations in all other scatter plots C_{ii}—C_v and for (D) the corresponding dSTORM image. Pearson correlation values of the data in panel C are shown in table S1.

cell footprint. Interestingly, red dots in figures 3(A) and (B) correspond to a subpopulation of localizations, having high σ and high intensity and likely represent aggregates or miss-localizations due to high density of emitters. We further demonstrate the ability of SOFI to distinguish aggregates in the last section of the results.

Since multiple ways to reconstruct and render SMLM images have been proposed [21], we clarify below our approach for SMLM reconstruction and rendering. First, in this work we selected the SMLM reconstruction algorithm based on its high-performance in a published comparison of SMLM reconstruction algorithms [21]. We also tested for this study multiple SMLM reconstruction parameters that were recommended for the algorithm (see SI). Second, we occasionally rendered the SMLM images (e.g. in figures 3(B), (D)) as scatter plots of the localized emitters. This way *intentionally* emphasizes the abundance of false localizations in relation to true localizations. Note that such false localizations are often less evident by the typically used rendering of summed Gaussians of detected molecules (compare figures 3(B), (D) with the corresponding images in figures 1(A), (B), at 400 or 1200 frames). Naturally, false localizations affect the calculated SNR (and ASNR or any other quantitative analyses) regardless of their appearance. Thus, our quantitative analyses throughout the study are independent of the rendering method, and are aimed to enhance SMLM reconstruction beyond overall image appearance, as described below.

SOFI-assisted PALM reconstruction

Experimental data often suffers from significant background (auto-fluorescence), out-of-focus background, varying concentrations of fluorophores within the same field of view (FOV), complicated and heterogeneous photophysical properties of fluorophores, cellular dynamics (when imaging live samples), and detector and read-out noise. These factors often complicate the localization of single fluorophores, as in the case of PALM and dSTORM, and may affect SMLM detection fidelity [22]. As a result, optimization of localization parameters is often required in order to maximize the detection probability of single emitters ($P_d \overset{def}{=\!=} \frac{\text{detected flourophores}}{\text{total \# flourophores}}$) and minimize the probability of false detection ($P_{fd} \overset{def}{=\!=} \frac{\text{false detections}}{\text{total \# detections}}$). We argue that the temporal correlation of a single emitter signal (encoded as a SOFI pixel value) can assist in accepting or rejecting a peak localization event (figure 3). To test this approach, we developed a realistic simulator and critically tested SOFI-assisted background rejection on simulated data (as described below and in SI-2).

Realistic simulations for fluorescence imaging

In SMLM imaging, it is often hard to validate the molecular detection and localization results, as the positions of emitters are not a-priori known. Simulated data provides ground-truth information that background rejection algorithms can be tested against. We therefore developed a simulator for fluorescence microscopy imaging data (available at www.github.com/xiyuyi/RealisticSimulator_3D). The simulations encoded realistic point spread function (PSF) based on Gibson & Lanni's model [23]. The simulation also modelled TIRF or epi illumination, as well as shot noise and a realistic pixel size to model detection optics and camera. The simulator also allows for the inclusion of different emitter types (emission wavelength and photophysical properties), different density and binding uncertainties of emitters to feature of interest, variable sample background, out-of-focus light, sample auto-fluorescence and bleaching dynamics. All parameters could be included and adjusted to simulate real data sets and imaging conditions (see figure S3 and SI-2 for further details). The simulator provides a powerful tool to generate a dataset library covering various experimental conditions. In turn, background rejection algorithms can be tested against large parameter space and compared to the ground-truth, allowing for their optimization and refinement. We note that other simulations of fluorophores have been introduced for SMLM and SOFI [9]. However, control over some relevant parameters, such as variable background, was absent in the published simulations and have been important for the quantitative evaluation of our approach, as follows.

Automatic determination of the detection threshold

Image reconstruction of SMLM images often employs subjective thresholding to identify single emitters and to reject the surrounding background [21] (however, see [24]). The simulator allowed us to develop an objective and automated thresholding algorithm, by providing simulated movies of emitters with known locations (ground-truth) and photophysical properties on realistic background. As a representative dataset, we simulated single emitters that highlighted a 3D (or 2D) tubulin-like mesh and included realistic background components (see figures 4(B), S3(A), (B) and SI for further details on simulation parameters). We then analysed the dataset using SMLM and SOFI and plotted histograms of SOFI (figure 4(A)) or sum-intensity (figure S3(A)) values of all pixels in the images. We found a distinct sub-population of background pixels (having the lowest values) in the log-normal histogram (figure 4(A)). This grouping of pixels into a distinct background subpopulation was robust to various simulated parameters, including imaging in 3D and 2D (figure S3), and could not be achieved by using only the sum image (compare figures 4(A) and S5(A)). Importantly, this grouping enables us to systematically detect the background peak in the histogram and fit it with a Gaussian. Next, a user-defined threshold could be placed based on

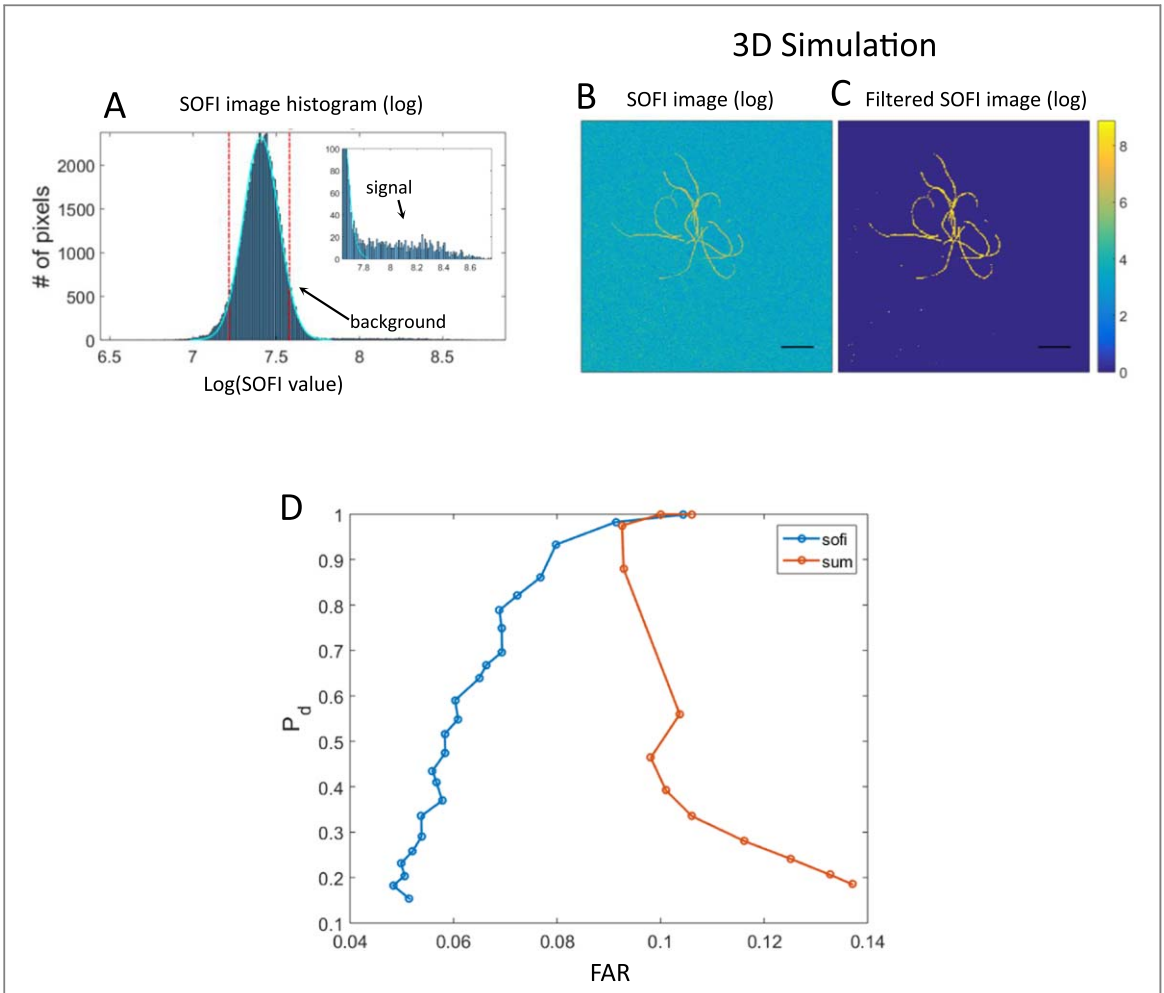

Figure 4. Automatic thresholding for background rejection in simulated SMLM data. (A) The log-normal histogram of SOFI values for 3D simulated data. A threshold was automatically set based on Gaussian fitting of the left-most peak in the histogram. Dashed red lines indicate the detected mode of the distribution, but not the applied threshold. (B) The SOFI image of the simulated data. (C) The SOFI image of the simulated data after automatic thresholding of SOFI values. (D) Analyses of background rejection represented as the detection probability (P_d) vs the false alarm ratio (FAR) for the simulated and automatically filtered data in panels A-C and figures S5(D)–(F) (SOFI based filtering in blue, sum image based filtering in red).

SOFI values (see further details in SI-1.7). This threshold formed a spatial mask that efficiently isolated the fraction of ground-truth emitters (i.e. the true signal) in the SMLM image, while allowing a predetermined percentage of background-originated false-positive detections, i.e. false SMLM localizations, to 'leak' through the mask (compare panels B and C in figure 4). This fraction of false-positive detections is typically referred to as the probability of false-alarms ($P_{fa} = \frac{detected\ background\ emitters}{Total\ background\ emitters}$). Similar masking based on a sum-image threshold (figures S5(B) and (C)) resulted in a wider and less efficient background rejection as compared to SOFI-based masking. To quantify the performance of background rejection, it is useful to define the false alarm ratio (FAR) of the mask, as $FAR = \frac{detected\ background\ emitters}{Total\ detected\ emitters}$ (see section 1.7.4 in the SI). We then compared the Pd as a function of FAR using either SOFI-based masking or sum-image-based masking and a range of threshold values. Lowering the SOFI threshold increased the FAR while increasing the Pd, i.e. increasing the detected fraction of ground-truth emitters (figure 4(D), blue line). In contrast, masking the SMLM image by setting a threshold on the sum-image achieved inferior Pd versus FAR curves in comparison to the SOFI-based approach (figure 4(D), red line). High detection probability can be achieved by a sum-image mask, however it undesirably increases the probability false-alarms. Moreover, the Pd versus FAR curve for the sum image masking is not monotonous since the sum-image mask confuses signal pixels with background pixels (e.g. compare figures S5(B) and (C)). We conclude that sum-image masking shows consistently an inferior background-rejection capability, in comparison to SOFI-based masking.

More appropriate approaches for comparison with our SOFI-based filtering approach include median filtering [22] and 'local density filtering' (e.g. [25]). We applied these methods to our data (figure S6). In our comparison, 'median filtering' missed a large

fraction of signal for PALM (figure S6(B), top) and left much of the background for dSTORM (figure S6(B), middle). It also left some background in the simulated data, but identified aggregates well (figure S6(B), bottom). A notable difference between this approach and ours includes an assumption of imaging sparse emitters by 'median filtering', which is not needed by our approach. The 'local density filtering' approach nicely reduced background for PALM (figure S6(C), top) and dSTORM (figure S6(C), middle) with some loss of signal. For the simulated data, it showed robust detection of filaments and aggregates, but failed to ignore out-of-focus background, which resulted in thicker microtubules and thus, a significant loss in resolution (figure S6(C), bottom). Also, local density filtering requires a density-dependent threshold that is not needed in our approach. It is thus optimal for rejecting isolated detections as a common source of background. This often results in the false rejection of single isolated emitters in the cell footprint, especially of monomeric fluorophores. Also, this method cannot readily reject aggregates outside of the cell footprint, as demonstrated via our approach (figure S6(C), top). Thus, we conclude that our SOFI-based approach for background rejection is conceptually different than previous algorithms and that it naturally captures differences between background and fluorophores, and between monomers and aggregates.

Importantly, the SOFI-based spatial mask could be used to significantly accelerate SMLM image reconstruction, since the computationally demanding task of peak identification and fitting could now be focused on a small part of the imaging field. For instance, we found that SOFI based filtering of simulated SMLM data (figure 3(D)) that was set for a *FAR* of 0.8% could achieve a P_d of 93.3% with a mask size of only 2.6% of the imaged field. We demonstrate in a later section the results the SOFI-assisted acceleration of SMLM reconstruction.

Our SOFI-assisted SMLM was not intendent for improvement of imaging resolution. Still, the ability of SOFI to reject common sources of background may improve the overall ability to resolve continuous features in areas where they are obscured by various background sources. To quantify such possible improvement, we employed the FRC statistics [26, 27]. This statistics was employed to correlate simulated, ground-truth emitters placed on microtubule-like structures (figure S4(A)) to their decoded images via either SOFI, SMLM or SOFI-assisted SMLM. The FRC of the SOFI-assisted SMLM approach showed consistently improved resolving capability in comparison to both SOFI and SMLM (figures S4(B), (C)). A resolution criterion where the FRC drops to $1/7$ was used, where f_c is the cut-off frequency [28]. The spatial resolution is then determined to be $0.5/f_c^{-1}$. The FRC analysis indicated an average resolution improvement over the entire image of $\sim 7 \pm 1\%$ by SOFI-assisted SMLM (at 51 nm), in comparison to SMLM (at 54 nm). In some cases, we note an improvement of $>33\%$ in resolution (e.g. figures S4(B), (C); Resolution of 40.5 nm for SOFI-assisted SMLM versus 52 mn for SMLM). As expected, these cases occur at the edges of the SOFI mask where an edge of a continuous feature is detected. Thus, SOFI-assisted SMLM may have a modest, yet significant, enhancement to SMLM resolution.

Cross-correlation of signal between pixels or Fourier-interpolation has been introduced to SOFI reconstruction for enhancing its resolution [29, 30]. As expected, applying such interpolation to the 3D simulated data (figure 4(B)) during the creation of our SOFI masks resulted in tighter and more optimal mask. This mask had only 60% of the areal size of the regular SOFI-based mask (figure S5(J)). Although we typically did not apply cross-correlation SOFI in our study, it can be readily combined with our approach and result in tighter, and more optimal SOFI-based masks.

Dynamic optimization of SMLM reconstruction

We next applied our SOFI-assisted SMLM image reconstruction to experimental data, acquired by PALM (figures 5(A)–(C)) and dSTORM (figures 5(D)–(F)). In both cases we found that automatic SOFI-based thresholding and detection showed efficient background rejection that could not be obtained by sum-image based thresholding (figures S5(D)–(J), and as shown earlier for the simulated data in figures S5(A)–(C)). So far, we have presented results for fixed cells. In order to employ our technique of SOFI-assisted background rejection to SMLM of live cells, we first needed to evaluate the speed by which the SOFI mask converges. For that, we first calculated the P_d of a SOFI mask that was dynamically updated during image acquisition of simulated 3D data (figure 6(A); simulated data shown in figure 4(B)). The SOFI mask was updated using a threshold for allowing a constant fraction (5%) of background pixels of the SOFI histogram. The SOFI mask was calculated for a sliding time window of 100 frames with time steps of 40 frames (as in figure 4(A); for a detailed discussion see SI-1.7.4). We found that the SOFI mask converged quickly relative to the movie length, jumping from a P_d value of $\sim$0.55 to $\sim$0.87 within 80 frames, and saturating at $\sim$0.93 after 200 frames. Thus, we conclude that using SOFI mask over 100 frames around each time point could provide an efficient way of background rejection in live cell SMLM. To demonstrate the effectiveness of our approach, we employed a dynamic mask, calculated every 100 frames, to PALM images of a representative live T-cell expressing TCRζ-Dronpa and spread on an αCD11a-coated coverslip. The sequences of original and SOFI-

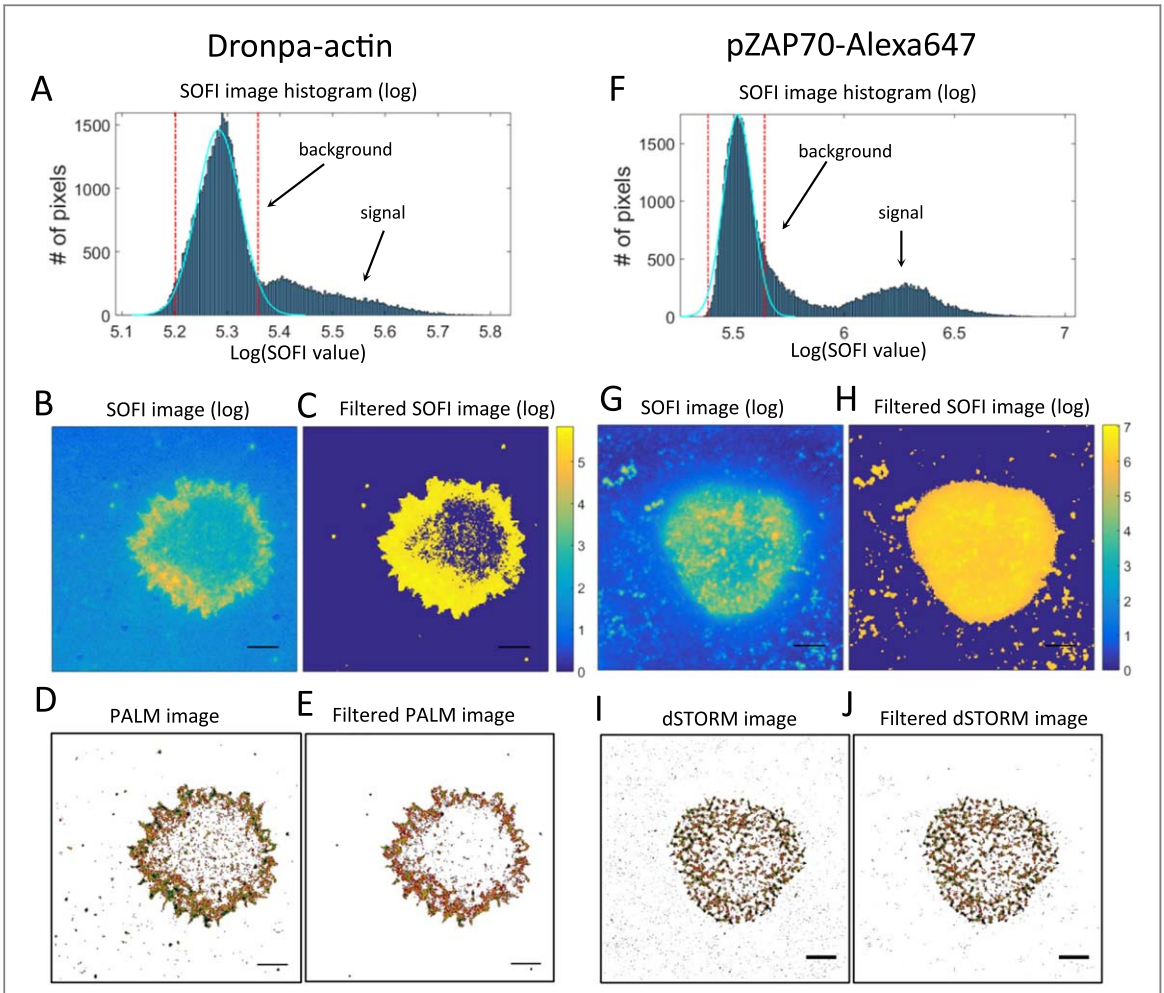

Figure 5. Efficient filtering of SMLM detections using SOFI. (A) The histograms of SOFI log-values for PALM imaging of a representative T cell expressing Dronpa-actin. A threshold of SOFI value was automatically set based on Gaussian fitting of the left-most peak in the histograms. This threshold formed a spatial mask that excluded all SMLM localizations that were within pixels of SOFI values lower than the threshold, while allowing a 5% background fraction to 'leak' into the image. (B) The SOFI image of the cell. (C) The filtered SOFI image of the cell. (D) The histograms of SOFI log-values for dSTORM imaging of a representative T cell stained for αpZAP70. A threshold was automatically set based on Gaussian fitting of the left-most peak in the histograms, as explained for panel A of this figure. (E) The SOFI image of the cell. (F) The filtered SOFI image of the cell. Dashed red lines in panels A and F indicate the detected mode of the distribution, but not the applied threshold.

filtered PALM images are shown in figure 6(B) and supplemental movie M1, demonstrating efficient background rejection by the dynamic SOFI masking, even when significant spatial-temporal dynamics appears in the data. The fastest dynamics that can be achieved by our technique is limited by the number of frames per block needed to construct the SMLM image (approximately 220 frames in figure 6(B)), rather than the relatively faster SOFI mask calculation (of 100 frames). Notably, SOFI-assisted rejection of background significantly narrowed the size of features (compare insets of images in top versus middle row in figure 6(B) and intensity profiles at the bottom row).

SOFI-assisted SMLM reconstruction improves optical sectioning

We next demonstrate how SOFI can assist in SMLM reconstruction under challenging conditions. We conducted live cell imaging of an immune synapse formed between a $CD8^+$ T cell and a T2 hybridoma cell that acts as an antigen presenting cell (APC) (figure 7, Movie M2). The TCRs on the $CD8^+$ T cells specifically recognize the NY-ESO-1 peptide that was first loaded on the APC [31]. Both cells were stained using a primary antibody against CD45, while the secondary staining used two different labels (Alexa488 or Alexa647) for highlighting the different cells. This system is challenging for imaging using either diffraction-limited (figure 7(B)) or SMLM (figure 7(C)) microscopy, as some features that facilitate the contact (here lamellae as an example) are overwhelmed by the background from molecules at the PM, out-of-focus light and cell auto-fluorescence. Here, SOFI filtering allows for efficient background rejection (mostly out-of-focus light) and the identification of faint lamellae that mediate the inter-cellular contact (figure 7(D)) at a plane ~5 μm above the coverslip.

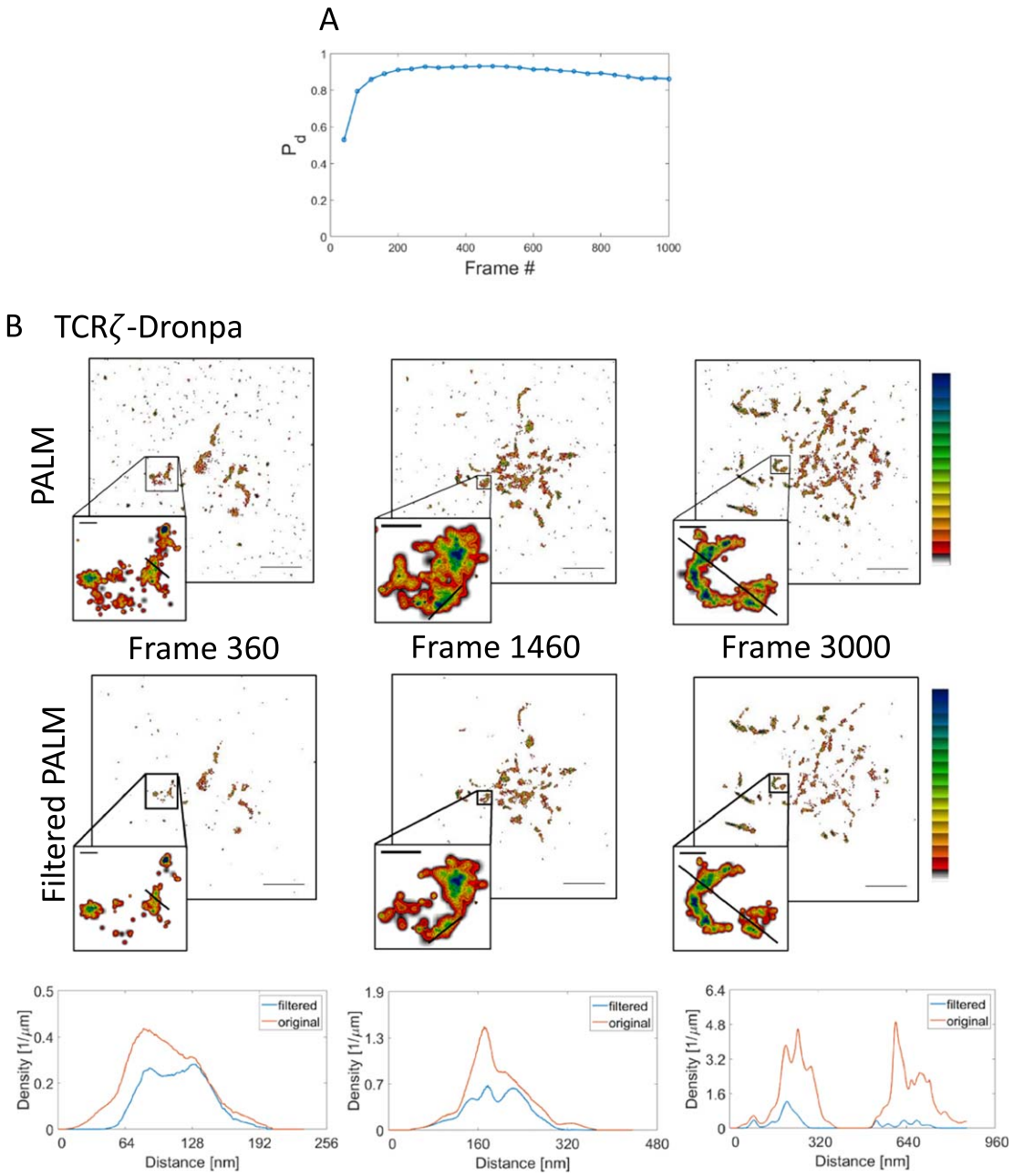

Figure 6. SOFI-assisted SMLM image reconstruction of live cell imaging. (A) The probability of detection of a SOFI mask that is dynamically updated during image acquisition of simulated 3D data (shown in figure 4(B)). The SOFI mask was calculated for a sliding window of 100 frames with time steps of 40 frames. The SOFI value threshold for the mask was defined for allowing 5% background fractions (as in figure 4(A); see further details in the Materials and Methods). (B) Unfiltered (top row) and SOFI-assisted filtered (middle row) PALM images of a representative T-cell expressing TCRζ-Dronpa and spread on an αCD11a-coated coverslip. Presented images show the build-up of higher resolution images over the acquisition time of 50 frames/s (10 ms exposure time). Insets show zoomed regions where out-of-focus background broadens the cell features in the unfiltered images. Intensity profiles of features in the insets (black angled lines in the insets) are shown in the bottom row. Bars—5 μm (full image) and 0.5 μm (insets). Colour bars for top row images (left to right)—0 to 16592, 4463, or 30984 localizations/μm^2. Colour bars for middle row images (left to right)—0 to 5554, 3311, or 3485 localizations/μm^2. Each image in the time series is the sum of 100 single frames analysed by ThunderSTORM and SOFI filtered as described above for live cells.

SOFI enables density-dependent SMLM reconstruction and reconstruction speedup

We further show the ability of SOFI to quickly identify areas of high molecular density in simulated data using Dronpa statistics (compare figures 8(A) and (B)) [32]. We note that multiple factors can affect the capability of SOFI to correctly assess the density level of emitters in each pixel, including their local blinking behaviour and their quadratic dependence of emitter brightness. These factors lead to the broadening of the correlation (i.e. of the scatter plot in figure 8(C)) between SOFI values and the local density of emitters.

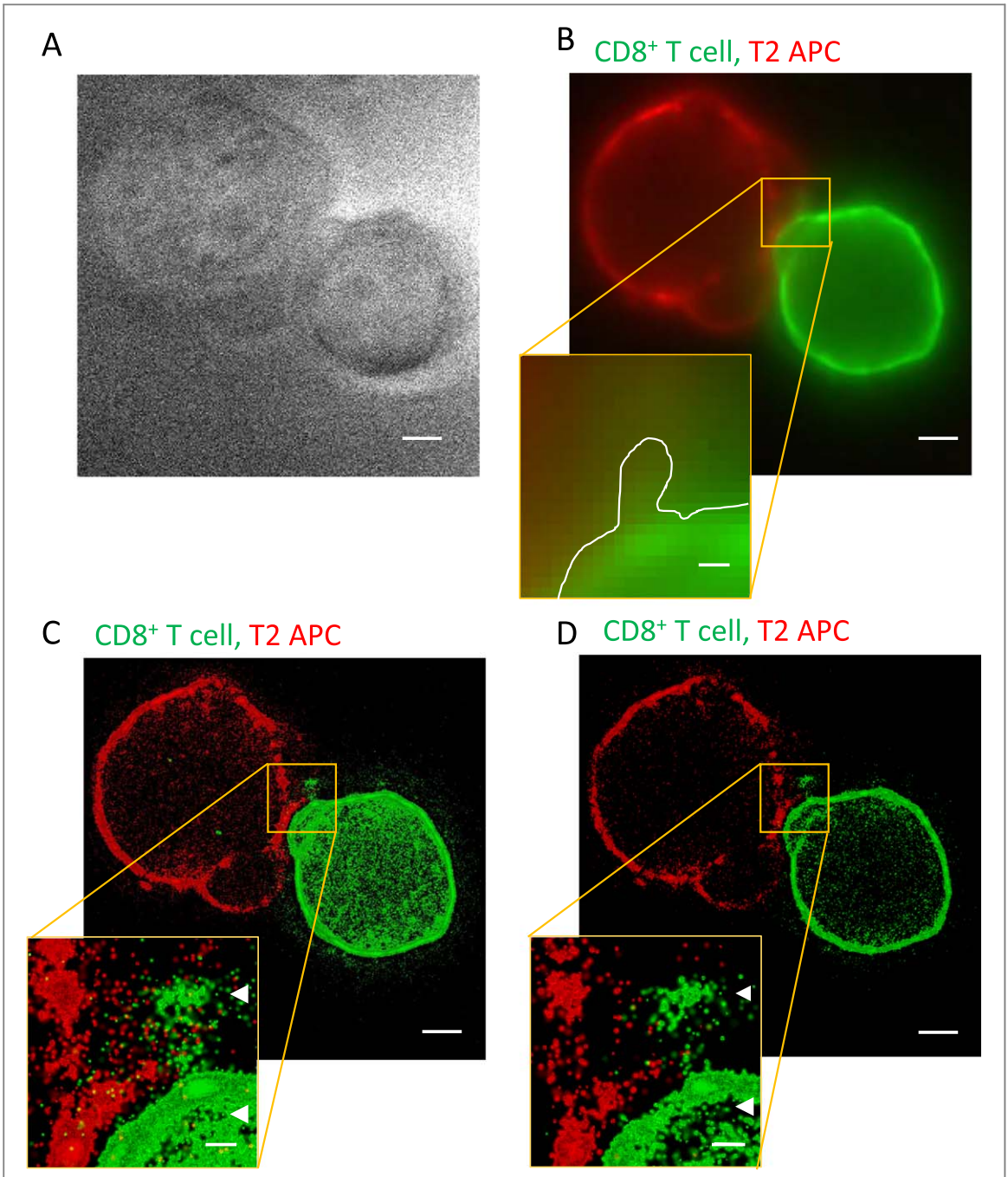

Figure 7. SOFI-assisted optical-sectioning and SMLM image reconstruction of an immune synapse. Representative images of an immune synapse between live cell conjugates of a $CD8^+$ T cell (in green) and a T2 (in red) that acts as an antigen presenting cell (APC). The TCRs on the $CD8^+$ T cells recognize the NY-ESO-1 peptide that was loaded on the APC first ($N = 14$). Both cells were stained using a primary antibody against CD45, while the secondary staining used two different labels (Alexa488 or Alexa647) for highlighting the different cells. (A) The bright-field image. (B) The sum-intensity image. (C) The SMLM reconstructed image. (D) The SMLM reconstructed image after SOFI-assisted filtering. Zoom images in B-D show a region of interest where a lamellae (in green) mediate the inter-cellular contact. The interface between the cells is marked by a dotted white line. An open arrow in panel C indicates the lamellae, masked by background detections from out-of-focus light. A filled arrow in panel D indicates the lamellae after background removal by SOFI-assisted filtering. Bars –2 μm (full images) and 500 nm (insets).

The ability of SOFI to locally asses the emitter density can be utilized to focus the computationally demanding effort of multiple peak fitting in SMLM reconstruction to areas of high emitter density. Single peak fitting is then performed outside of these regions where the emitter density is low.

We further show for simulated 3D data with high background (figures 8(D) and (E)) that multiple peak fitting to the whole image for SMLM reconstruction grows exponentially in computation time (figure 8(F); see section 1.7.6 in the SI for further details). The ratio between the computation time of single emitter fitting to six emitter fitting is 33 ± 3. The focusing of multiple peak fitting only to regions of high molecular densities reduces the computation time by a factor given by the following relations:

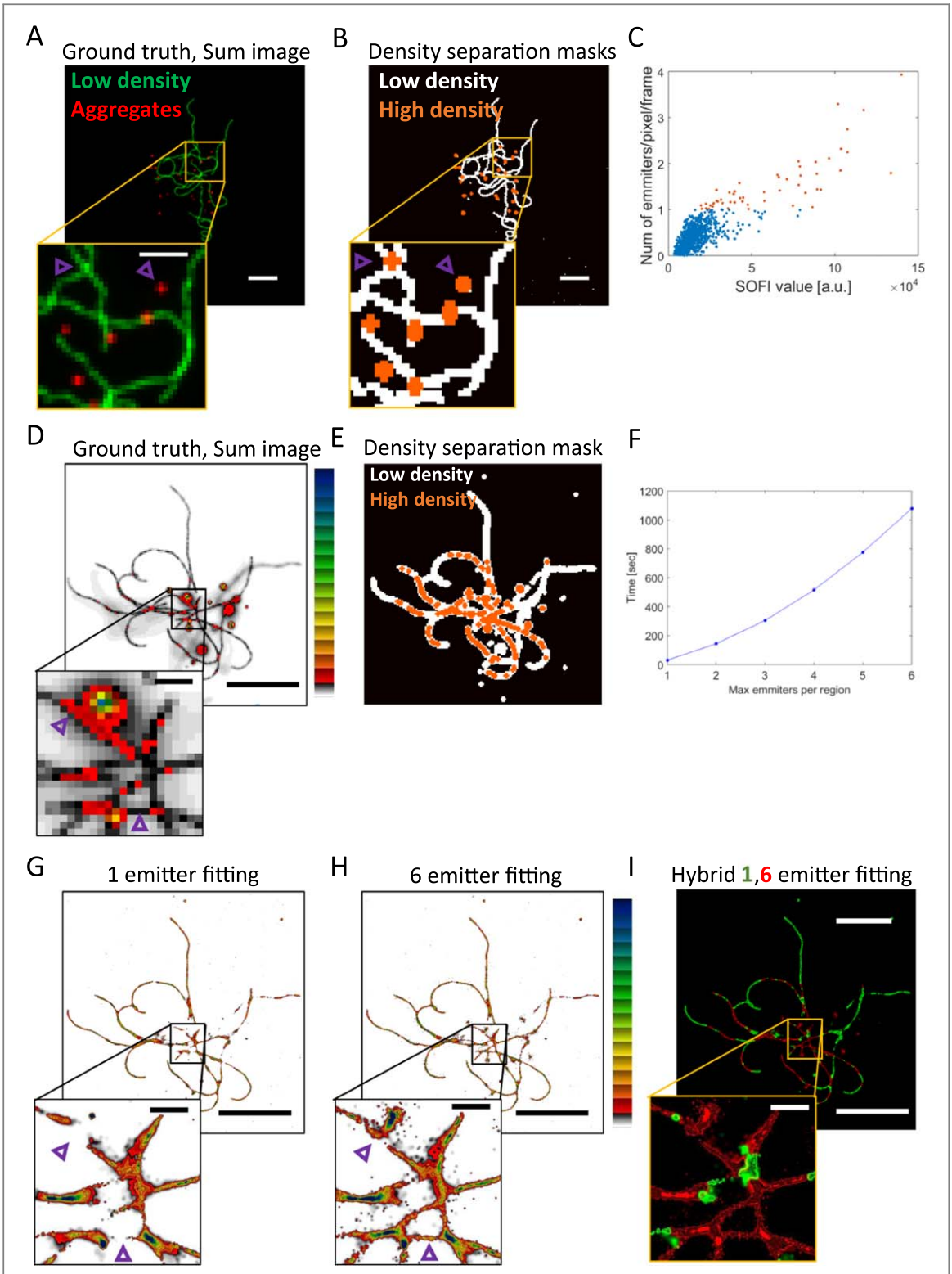

Figure 8. SOFI-assisted speedup of SMLM image reconstruction with multiple peak fitting. (A) Sum image of 2D simulated data without noise of single emitters (green) and aggregates (red). (B) Density separation masks (data of A) of low (white) and high (orange) density areas. Purple arrows in zoom regions of panels A and B indicate high density features (aggregates and microtubule crossings) that are correctly detected by the density separation mask. (C) The number of emitters per pixel per frame versus the pixel SOFI value. Pixels with low density of < 1 emitters/pixel/frame are shown in blue and pixels with high density of emitters of >1 emitters/pixel/frame are shown in orange. (D) Sum image of 3D simulated ground truth without noise. (E) Density separation masks (data of D) of low (white) and high (orange) density areas. (F) The SMLM reconstruction time of the data using different maximal number of fitted emitters per region in ThunderSTORM (see SI-1.7, 1.7.6 for further details). (G) The reconstructed SMLM image of the cell using single peak fitting. (H) The reconstructed SMLM image of the cell using 6 peak fitting. (I) The reconstructed SMLM image of the cell using 6 peak fitting in the high density regions in red (orange regions in panel E) and single peak fitting in low density areas regions (in green; white regions in panel E). Bars –5 μm (full image) and 500 nm (insets). Purple arrows in zoom regions of panels D, G, H indicate high density features that are missed by single-emitter fitting (panel G) but correctly detected by 6 emitter fitting (compare panels D, H).

$$speedup = \frac{(A_{LD} - A_{HD}) \times T_1 + A_{HD} {}^{*} T_{6\ \mathrm{emitter}}}{A_{LD} \times T_6} \times \underset{T_1 \ll T_6}{\approx} \frac{T_1}{T_6} + \frac{A_{HD}}{A_{LD}} \quad (3)$$

Where T_1, T_6 are the times of single and six emitter fitting, A_{HD}, A_{LD} are the areas of high and low density of molecules where the fitting is performed. We show that our approach results in efficient identification of single emitters in high-density regions using minimal computation time (compare the images shown in figures 8(G)–(I)).

Discussion

SMLM and SOFI can both work with wide-field imaging configuration and use the reversible blinking of fluorophores for generating super-resolved images. Still, these two imaging methods differ in their reconstruction process of features of interest. SOFI collects values of intensity cumulants as an input. These values originate from both signal and background in each pixel. In contrast, SMLM collects the intensity of sparse fluorophores. Over time, detected emitters are collected to reconstruct features of interest. Importantly, during this process, background can be collected as false detections, from each pixel across the object of interest. To compare the two methods, we introduced a measure dubbed 'acquired SNR' (ASNR). SOFI shows 10 to 100 fold better ASNR values when compared to SMLM. Thus, ASNR, by its construction, highlights the faster acquisition rate and possible reconstruction speed of SOFI in comparison to SMLM.

In addition, for static features, ASNR allowed us to optimize the time-lags used in correlation calculations to optimize the SOFI reconstruction, and for dynamic features, ASNR further allowed us to identify optimal time lag for SOFI reconstruction to achieve desired temporal resolution. Importantly, this approach can be used in future studies to optimize SOFI reconstruction. Thus, it may become especially important under stringent experimental conditions such as live-cell imaging, using dim emitters, 3D imaging etc.

We are not aware of similar time-lag optimization of SOFI reconstruction in previous studies, which always used $\tau = 0$ (e.g. [8, 9, 19]). Deschout *et al* [19] optimized the time-dependence of SOFI versus PALM reconstruction for live cell imaging. They found that PALM becomes favourable over SOFI after imaging times of 1000–2000 frames, while at shorter times, SOFI is favourable. Thus, they recommend to display a hybrid image of SOFI and PALM at short acquisition times. However, the SNR statistics used in their study was calculated from the final image (Step 3 in figure 2(A)). Such statistics highly depend on subjective thresholding and may substantially vary between imaging conditions, fluorophores and reconstruction approaches. In contrast, our analyses show that SOFI has a significantly higher ASNR than SMLM, and hence can detect relatively faster movements of features within the resolution limit of SOFI. Namely, the detection of smaller features would benefit from the enhanced resolution of SMLM, but will be limited by the lower resolution of SOFI. Notably, ASNR statistics does not operate on the processed signal and related background (step 2 in figure 2(A)) and does not rely on non-linear thresholding of the background.

Next, we performed SOFI and SMLM image reconstructions on the same data-sets and compared SOFI values (2nd order auto-correlation) and the output parameters from SMLM [13]. We identified that SOFI values were largely uncorrelated (and thus complementary) to SMLM output parameters, and, and that it provided an effective background rejection capability. These properties offer the opportunity to combine SMLM with SOFI image reconstruction for optimized SMLM performance. Benefits of SOFI-assisted SMLM image reconstruction include: efficient background rejection and optical sectioning with automatic thresholding, isolation of emitter subpopulations, and acceleration of SMLM image reconstruction. In contrary to earlier studies that focused on the comparison of SOFI and SMLM [9, 19] and their separate reconstruction and alternating rendering during an imaging sequence [19], our approach emphasizes on the integration of SRM imaging techniques with the resultant benefits.

To demonstrate the applicability of our approach, we applied it to both PALM and dSTORM experimental data. For that, we imaged fixed and live Jurkat T cells and the immune synapse between $CD8^{+}$ T cells with APCs. SOFI and dSTORM have been previously compared under various fluorophores blinking statistics [9] and SMLM was compared under different labelling density conditions [21]. Thus, our integrated reconstruction approach was applied to various PALM and dSTORM labels of multiple target proteins. In our study, we also developed a realistic simulator for wide-field fluorescence imaging to critically evaluate the performance of our approach and to develop automatic SOFI-based thresholding for SMLM (given a user-defined P_{fa} threshold). Our algorithms and simulations are available online (see links in the Materials and Methods below and in SI-2.1).

The contribution of our combination of SMLM and SOFI can be separated into different region of an image, containing either background alone or signal and background (e.g. figure 2(B)). In areas where there is only background, the SOFI mask efficiently rejects false localizations that would otherwise take computational resources (e.g. time) for detection and analysis. In areas that contain signals of interest (e.g. cell footprints), the mask is limited by SOFI resolution. Thus, we expect (and observe) that the background-induced smearing of SMLM features would shrink by a factor that is limited

by the SOFI resolution (following the $\sqrt{2}$ reduction of the PSF radius by ***2nd*** order SOFI). Importantly, tighter and more optimal masks can be generated by enhancing SOFI resolution, e.g. via higher-order SOFI reconstruction or by using SOFI interpolation, as demonstrated here (figure S5(J)). More generally, our filtering approach differs conceptually from previous approaches as it naturally distinguishes between signal and background emitters. In comparison to two published algorithms, namely median filtering [22] and local-density filtering [25], it showed a more robust rejection of diffused and aggregated background outside the cell footprint, and of out-of-focus background within this footprint (figure S6).

Both high-order SOFI and SMLM image reconstructions are computationally expensive. Indeed, high-order SOFI reconstruction may provide tighter and more optimal masks, yet it requires more frames for reconstruction relative to 2nd order SOFI. The availability of the required frame number for reconstruction may become problematic in live cell imaging. Nevertheless, the computationally inexpensive 2nd order SOFI is already sufficient for efficient background rejection. We also demonstrated how the fast identification of regions of high molecular density by SOFI [32] can be employed to focus demanding computational effort of multiple peak fitting to dramatically reduce SMLM reconstruction time, while preserving optimal performance of peak identification. With further improvements in computer hardware, the development and implementation of more optimal and cost-effective SMLM and SOFI algorithms and their possible implementation in hardware (such as graphical processing units, GPUs) will facilitate faster and possibly even real-time image reconstruction of the SOFI-assisted SMLM technique [33].

The lack of correlation between SOFI values and SMLM output parameters indicates a more general aspect of image acquisition. It demonstrates that every imaging technique is only an estimated version of the true data and carries with it its own set of characteristics artefacts. For instance, the detection of SMLM peaks and their fitting with Gaussians introduce errors and artefacts. SOFI image reconstruction requires a different set of information (intensity fluctuations) and considerations. Thus, the artefacts generated by either technique can be compensated for (and possibly corrected) by tracing back the loss or distortion of information by each technique. Synergic combinations of different imaging reconstruction approaches have been demonstrated before [34]. Our approach is a specific example for the synergetic combination of additional SRM and diffraction-limited imaging techniques.

Our approach for combining SMLM and SOFI may be expanded in the future. For instance, it can enable the usage of variable PSF parameters, background estimators and local threshold criteria for peak detection in cases of uneven illumination or highly varying background in space and time. Also, the ability of SOFI to assess local emitter density may be used to automatically diagnose regions containing fitting artefacts in single emitter fitted SMLM data.

In conclusion, the merging of the techniques described herein improves SMLM image reconstruction, and provides tools for the evaluation, comparison and synergistic combination of SOFI and SMLM.

Competing financial interests

The authors declare no competing financial interests.

Acknowledgments

The authors would like to thank Oreste Acuto and Andre Cohnen (Oxford University, UK) for kindly providing us the CD8 + and T2 cells and Yonatan Golan for fruitful discussions. The authors acknowledge support by Grant no. 321993 from the Marie Skłodowska-Curie actions of the European Commission, the Lejwa Fund (to E S), Grants no.1417/13 and no. 1937/13 from the Israeli Science Foundation (to E S), National Science Foundation Grant No. DMR-1548924 (to S W) and Willard Chair funds (to S W).

Contributions

E S, S W, S S, and X Y designed research, S S, Y R, and J S performed experiments, S S analyzed data, X Y developed simulations, S W and E S supervised the research and E S wrote the manuscript.

ORCID iDs

Eilon Sherman https://orcid.org/0000-0002-7403-6036

References

[1] Hell S W 2007 Far-field optical nanoscopy *Science* **316** 1153–8
[2] Betzig E *et al* 2006 Imaging intracellular fluorescent proteins at nanometer resolution *Science* **313** 1642–5
[3] Rust M J, Bates M and Zhuang X 2006 Sub-diffraction-limit imaging by stochastic optical reconstruction microscopy (STORM) *Nat. Methods* **3** 793–5
[4] van de Linde S *et al* 2011 Direct stochastic optical reconstruction microscopy with standard fluorescent probes *Nat Protoc* **6** 991–1009
[5] Hell S W and Wichmann J 1994 Breaking the diffraction resolution limit by stimulated emission: stimulated-emission-depletion fluorescence microscopy *Opt. Lett.* **19** 780–2
[6] Gustafsson M G L 2000 Surpassing the lateral resolution limit by a factor of two using structured illumination microscopy *Journal of Microscopy-Oxford* **198** 82–7
[7] Gustafsson M G 2005 Nonlinear structured-illumination microscopy: wide-field fluorescence imaging with theoretically unlimited resolution *Proc. Natl Acad. Sci. USA* **102** 13081–6
[8] Dertinger T, Colyer R, Iyer G, Weiss S and Enderlein J 2009 Fast, background-free, 3D super-resolution optical fluctuation imaging (SOFI) *Proc. Natl Acad. Sci. USA* **106** 22287–92
[9] Geissbuehler S, Dellagiacoma C and Lasser T 2011 Comparison between SOFI and STORM *Biomedical Optics Express* **2** 408–20
[10] Mukamel E A and Schnitzer M J 2012 Unified resolution bounds for conventional and stochastic localization fluorescence microscopy *Phys. Rev. Lett.* **109** 168102

[11] Ovesny M, Krizek P, Borkovec J, Svindrych Z K and Hagen G M 2014 ThunderSTORM: a comprehensive ImageJ plug-in for PALM and STORM data analysis and super-resolution imaging *Bioinformatics* **30** 2389–90
[12] Dedecker P, Duwe S, Neely R K and Zhang J 2012 Localizer: fast, accurate, open-source, and modular software package for superresolution microscopy *J. Biomed. Opt.* **17** 126008
[13] Bunnell S C, Kapoor V, Trible R P, Zhang W G and Samelson L E 2001 Dynamic actin polymerization drives T cell receptor-induced spreading: A role for the signal transduction adaptor LAT *Immunity* **14** 315–29
[14] Kaizuka Y, Douglass A D, Varma R, Dustin M L and Vale R D 2007 Mechanisms for segregating T cell receptor and adhesion molecules during immunological synapse formation in Jurkat T cells *Proc. Natl Acad. Sci. USA* **104** 20296–301
[15] Sherman E *et al* 2011 Functional nanoscale organization of signaling molecules downstream of the T cell antigen receptor *Immunity* **35** 705–20
[16] Gonzalez R C and Woods R E 2008 *Digital Image Processing* (Upper Saddle River, N.J: Prentice Hall) xxii, 954 p p
[17] Young I T, Gerbrands J J and van Vliet L J 1998 Image processing fundamentals ed V K Madisetti and D B Williams *The Digital Signal Processing Handbook* (Boca Raton FL: CRC Press) pp 01–51
[18] Vandenberg W *et al* 2016 Model-free uncertainty estimation in stochastical optical fluctuation imaging (SOFI) leads to a doubled temporal resolution *Biomed Opt Express* **7** 467–80
[19] Deschout H *et al* 2016 Complementarity of PALM and SOFI for super-resolution live-cell imaging of focal adhesions *Nat. Commun.* **7** 13693
[20] Pawley J B 2006 *Handbook of Biological Confocal Microscopy* (New York, NY: Springer) xxviii, 985 p. p
[21] Sage D *et al* 2015 Quantitative evaluation of software packages for single-molecule localization microscopy *Nat. Methods* **12** 717–U737
[22] Hoogendoorn E, Crosby K C, Leyton-Puig D, Breedijk R M P, Jalink K, Gadella T W J and Postma M 2014 The fidelity of stochastic single-molecule super-resolution reconstructions critically depends upon robust background estimation *Sci. Rep.* **4** 3854
[23] Gibson S F and Lanni F 1991 Experimental test of an analytical model of aberration in an oil-immersion objective lens used in 3-dimensional light-microscopy *J. Opt. Soc. Am. A* **8** 1601–13
[24] Smith C S, Stallinga S, Lidke K A, Rieger B and Grunwald D 2015 Probability-based particle detection that enables threshold-free and robust *in vivo* single-molecule tracking *Molecular Biology of the Cell* **26** 4057–62
[25] Jones S A, Shim S H, He J and Zhuang X 2011 Fast, three-dimensional super-resolution imaging of live cells *Nat. Methods* **8** 499–508
[26] Saxton W O and Baumeister W 1982 The correlation averaging of a regularly arranged bacterial-cell envelope protein *Journal of Microscopy-Oxford* **127** 127–38
[27] Banterle N, Bui K H, Lemke E A and Beck M 2013 Fourier ring correlation as a resolution criterion for super-resolution microscopy *Journal of Structural Biology* **183** 363–7
[28] Nieuwenhuizen R P J *et al* 2013 Measuring image resolution in optical nanoscopy *Nat. Methods* **10** 557
[29] Dertinger T, Colyer R, Vogel R, Enderlein J and Weiss S 2010 Achieving increased resolution and more pixels with Superresolution Optical Fluctuation Imaging (SOFI) *Opt. Express* **18** 18875–85
[30] Stein S C, Huss A, Hahnel D, Gregor I and Enderlein J 2015 Fourier interpolation stochastic optical fluctuation imaging *Opt. Express* **23** 16154–63
[31] Jager E *et al* 2000 Monitoring CD8 T cell responses to NY-ESO-1: correlation of humoral and cellular immune responses *Proc. Natl Acad. Sci. USA* **97** 4760–5
[32] Lukes T *et al* 2017 Quantifying protein densities on cell membranes using super-resolution optical fluctuation imaging *Nat. Commun.* **8** 1731
[33] Girsault A *et al* 2016 SOFI simulation tool: a software package for simulating and testing super-resolution optical fluctuation imaging *PLoS One* **11** e0161602
[34] Ingaramo M *et al* 2014 Richardson-lucy deconvolution as a general tool for combining images with complementary strengths *Chemphyschem* **15** 794–800